Journal of Modern Optics

ISSN: 0950-0340 (Print) 1362-3044 (Online) Journal homepage: https://www.tandfonline.com/loi/tmop20

Quenching of material dependence in few-cycle driven electron acceleration from nanoparticles under many-particle charge interaction

Philipp Rupp, Lennart Seiffert, Qingcao Liu, Frederik Süßmann, Byungnam Ahn, Benjamin Förg, Christian G. Schäfer, Markus Gallei, Valerie Mondes, Alexander Kessel, Sergei Trushin, Christina Graf, Eckart Rühl, Jinwoo Lee, Min Su Kim, Dong Eon Kim, Thomas Fennel, Matthias F. Kling & Sergey Zherebtsov

To cite this article: Philipp Rupp, Lennart Seiffert, Qingcao Liu, Frederik Süßmann, Byungnam Ahn, Benjamin Förg, Christian G. Schäfer, Markus Gallei, Valerie Mondes, Alexander Kessel, Sergei Trushin, Christina Graf, Eckart Rühl, Jinwoo Lee, Min Su Kim, Dong Eon Kim, Thomas Fennel, Matthias F. Kling & Sergey Zherebtsov (2017) Quenching of material dependence in few-cycle driven electron acceleration from nanoparticles under many-particle charge interaction, Journal of Modern Optics, 64:10-11, 995-1003, DOI: 10.1080/09500340.2016.1267272

To link to this article: https://doi.org/10.1080/09500340.2016.1267272

Published online: 25 Dec 2016.

JOURNAL OF MODERN OPTICS, 2017
VOL. 64, NOS. 10–11, 995–1003
https://doi.org/10.1080/09500340.2016.1267272

Taylor & Francis
Taylor & Francis Group

Quenching of material dependence in few-cycle driven electron acceleration from nanoparticles under many-particle charge interaction

Philipp Rupp[a,b], Lennart Seiffert[c], Qingcao Liu[a], Frederik Süßmann[a,b], Byungnam Ahn[d,e], Benjamin Förg[a,b], Christian G. Schäfer[f], Markus Gallei[f], Valerie Mondes[g], Alexander Kessel[a], Sergei Trushin[a], Christina Graf[g§], Eckart Rühl[g], Jinwoo Lee[h], Min Su Kim[h], Dong Eon Kim[d,e], Thomas Fennel[c,i], Matthias F. Kling[a,b] and Sergey Zherebtsov[a,b]

[a]Max Planck Institute of Quantum Optics, Garching, Germany; [b]Physics Department, Ludwig-Maximilians-Universität Munich, Garching, Germany; [c]Institut für Physik, Universität Rostock, Rostock, Germany; [d]Department of Physics, Center for Attosecond Science and Technology, Pohang University of Science and Technology, Pohang, Republic of Korea; [e]Max Planck POSTECH/KOREA Res. Init., Pohang, Republic of Korea; [f]Macromolecular Chemistry Department, Technische Universität Darmstadt, Darmstadt, Germany; [g]Physical Chemistry, Freie Universität Berlin, Berlin, Germany; [h]Chemical Engineering Department, POSTECH, Pohang, Republic of Korea; [i]Max-Born-Institut, Max-Born-Straße 2A, 12489 Berlin, Germany

ABSTRACT

The excitation of nanoscale near-fields with ultrashort and intense laser pulses of well-defined waveform enables strongly spatially and temporally localized electron emission, opening up the possibility for the generation of attosecond electron pulses. Here, we investigate the electron photoemission from isolated nanoparticles of different materials in few-cycle laser fields at intensities where the Coulomb field of the ionized electrons and residual ions significantly contribute to the electron acceleration process. The dependences of the electron cut-off energy on the material's dielectric properties and electron binding energy are investigated systematically in both experiments and semi-classical simulations. We find that for sufficiently high near-field intensities the material dependence of the acceleration in the enhanced near-fields is quenched by many-particle charge-interaction.

ARTICLE HISTORY
Received 15 October 2016Accepted 24 November 2016

KEYWORDS
Ultrafast nanophysics; carrier-envelope phase; nanoparticles; strong-field phenomena

Introduction

Intense laser pulses with well-defined waveform have proven to be a powerful tool for the creation, control and observation of sub-cycle electron dynamics in various systems ranging from atoms to solids. Ultrashort laser fields have been applied to drive and monitor attosecond controlled electric currents (*1*) and ultrafast, reversible modification of the bandstructure in dielectrics (*2*), bandgap dynamics in semiconductors (*3*), ultrafast metallization of dielectric materials (*4*), and are key to the realization of ultrafast dielectric electronics (*5*). Furthermore, attosecond light pulses have been used to probe electron transport in metals (*6*) and adlayer-metal systems (*7*). When intense fields are applied to nanostructured materials, enhanced and well-controlled near-fields can be excited, permitting tailoring optical fields on sub-wavelength spatial and attosecond temporal timescales (*8–14*).

The acceleration of photoelectrons emitted into intense tailored near-fields has been investigated for a variety of systems including isolated nanoparticles (*14–16*), metal nanotips (*12,17–20*) and surface-based nanostructures (*21,22*). Similar to atomic strong-field electron emission (*23*), the process in nanoscopic materials may be described by the Simple-Man's-Model (SMM) (*24*) as a three-step process that is driven by the enhanced localized fields (see e.g. (*12,16*)). The three steps involve (i) the multi-photon or tunnelling electron emission, (ii) its driven acceleration in the laser field and iii) a recollision process that can lead to further energy gain. At laser intensities where the ionization rate is relatively low, the near-field dynamics is mostly determined by the linear dielectric response of the nanosystem (*12*). For higher laser intensities, many-particle charge interaction of liberated electrons and residual ions can significantly modify the electron acceleration process and lead to quenching of the direct electron emission and extension of the cut-off energies beyond prediction of the SMM (*14*). The sub-cycle electron emission dynamics in the relevant intensity regime is largely unexplored as it remains an experimental challenge since charge generation from laser-induced damage

CONTACT Thomas Fennel thomas.fennel@uni-rostock.de; Sergey Zherebtsov sergey.zherebtsov@mpq.mpg.de
[§] Present address: Fachbereich Chemie- und Biotechnologie, Hochschule Darmstadt, University of Applied Sciences, Darmstadt 64289, Germany.

of the sample occurring on longer timescales obscures the observation of the laser-driven dynamics. Using few-cycle laser fields with controlled carrier-envelope phase (CEP) opens a route to isolate the ultrafast electron dynamics from slower processes (*15*) and extends the range of intensities that can be explored before the target is damaged (see e.g. (*25*)).

Here, we present results of our studies of the influence of the material properties, in particular permittivity and electron binding energy, on the laser-induced electron acceleration in nanolocalized fields at intensities where many-particle charge interaction is important. For this purpose, the waveform controlled electron emission from isolated, chemically synthesized SiO_2, polystyrene (PS), ZnS and Fe_3O_4 nanoparticles was studied at incident laser intensities of $(1–5) \times 10^{13}$ W/cm^2. The experimental results are compared to semi-classical Mean-field Mie Monte-Carlo (M^{3}C) simulations (*16, 26*), which have shown to provide accurate results for SiO_2 nanoparticles in earlier work. We find that for a sufficiently high dielectrically enhanced surface intensity the contribution from many-particle charge interaction quenches the material dependence in the electron acceleration.

Methods

Single-shot velocity map imaging of electron emission from isolated nanoparticles

The experimental setup is described in detail in (*15*). Briefly, intense laser pulses of 5 fs (intensity full-width-at-half-maximum) duration centred at 720 nm were focused into a nanoparticle beam inside a velocity-map imaging (VMI) spectrometer. In order to prepare the nanoparticle beam, the particles were brought into a gas stream of N_2 from suspension in ethanol by aerosol techniques (*27*), dried and focused with an aerodynamic lens, after which most of the residual gas was removed through differential pumping. For each laser shot, the projected momentum distribution of the electron emission from the nanoparticles (see Figure 1(a)) was detected with the VMI and the CEP of the few-cycle laser pulses was measured with a phase metre (*28, 29*). The single-shot detection allowed efficient suppression of background signal by neglecting electron momentum images that do not contain any nanoparticle signal (see (*30*) for more details). To determine the parameters of the laser field in the interaction volume (intensity and absolute CEP), above-threshold ionization (ATI) of Xe atoms was measured as a reference. The peak laser intensity was derived from the ATI spectral cut-off assuming the cut-off energy law $E_c = 10.007U_p + 0.538I_p$, (*31*) where $U_p = e^2E^2/(4m\omega^2)$ is the ponderomotive potential of an electron in the driving electric field E, and I_p is the ionization potential of the gas atoms. The nanoparticle samples were prepared by wet chemistry synthesis. Transmission electron microscopy (TEM) images of the samples were taken (see Figure 1(b)) to determine their shape and size distributions.

Nanoparticle synthesis and properties

The SiO_2 nanoparticle batches with 80, 92 and 110 nm diameter were prepared by wet chemistry methods based on the Stöber procedure and a seeded growth process (*32*). The polystyrene (PS) particles were prepared according to reference (*33*). In brief, the polymerization of a small amount of freshly distilled styrene in a deionized water

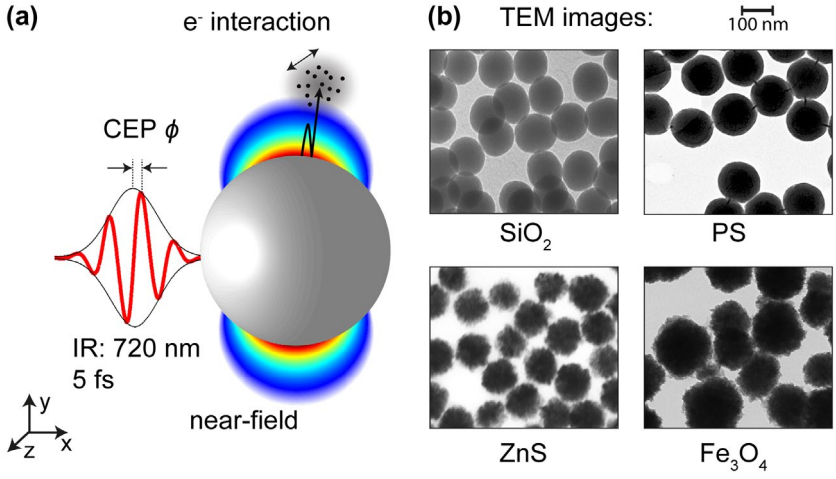

Figure 1. (a) Schematic of the experiment. The few-cycle laser pulse with CEP ϕ interacts with an isolated nanoparticle (e.g. 100 nm diameter, spherical SiO_2) and releases electrons that propagate under the influence of the local fields (the near-field of the nanoparticle and fields generated by charge interaction). (b) Representative TEM images of the investigated nanoparticles: SiO_2, polystyrene (PS), ZnS, and Fe_3O_4.

Table 1. Overview of parameters for the nanoparticle samples studied in this work. In measurements with SiO_2 nanoparticles three different samples of 80, 92, and 110 nm diameters were used, which yielded indistinguishable results. The field enhancement given in the table corresponds to the one obtained at the poles of spherical nanoparticles from the analytic Mie solution.

Material	Diameter (nm)	Nanoparticle binding energy (eV)	Bulk binding energy (eV)	Permittivity ε_r	Field enhancement a
SiO_2	(80–110) ± 8%	8.5 (*36*)	10.2 (*37*)	2.12	1.60
Polystyrene (PS)	111 ± 17%	5.0	6.1 (*38*)/6.95 (*39*)	2.50	1.76
ZnS	136 ± 33%	6.5	7.5 (*40*)	5.44	2.55
Fe_3O_4	150 ± 27%	6.5	5.8 (*41*)	5.86	2.67

emulsion acted as seed particles for the further growth process. More styrene was added over a period of 3 h. The resulting dispersion was further diluted with deionized water and the particle concentration was set to 2 g/l. The ZnS particles were prepared as previously described (*34*). The reaction of thioacetamide and $Zn(NO_3)_2{\cdot}6H_2O$ was carried out in deionized water. After 4 h of reaction time, the ZnS particles were purified by centrifuging and redispersing first in H_2O and then in ethanol for several times. The resulting dispersion was further diluted with ethanol and the particle concentration was set to 2 g/l. The Fe_3O_4 particles were prepared as follows. Ferric chloride hexahydrate ($FeCl_3{\cdot}6H_2O$) (0.12 M), sodium citrate dihydrate (0.01 M) and urea (1.0 M) were completely dissolved in ethylene glycol (30 ml). The solution was sealed in a Teflon lined stainless-steel autoclave (50 ml capacity) and then heated at 200 °C for 6 h. After cooling down to room temperature, the black sediment was separated magnetically, washed with ethanol and deionized water several times, and was then dried (*35*).

Table 1 lists the main properties of the studied samples. To avoid significant influence of field propagation effects (see e.g. (*16, 26*)), we used nanoparticles of diameters much smaller than the central wavelength of the laser pulses (*16*).

Trajectory simulations

The trajectory-based Mean-field Mie Monte-Carlo (M^3C) model (*16, 26*) was employed to describe the experimental results. In brief, the initial ionization step was approximated by the instantaneous atomic Ammosov–Delone–Krainov (ADK) tunnel ionization in the surface layer (*42*). In the simulations, we used the binding energy *BE* as the ionization potential as listed in Table 1 (see also (*43*)). After their ionization, electrons are propagated classically in the local near-fields, composed of the linear dielectric response of the sphere and taking into account charge interaction of the free electrons and the residual ions, cf. Figure 1(a). The linear near-field of the nanoparticle was calculated via the Mie solution of the Maxwell's equation for a sphere assuming constant relative permittivity of the respective bulk material. The charge interaction is approximated as an effective self-consistent mean-field and calculated via high-order multipole expansion. Electron scattering inside the nanoparticle was calculated assuming isotropic elastic scattering with the scattering parameters (cross section, mean free path) retrieved from quantum mechanical atomic scattering calculations. The elastic mean free path for the investigated energy range is similar for all materials. The inelastic mean free path was modelled with a simplified Lotz formula (*44*), which uses the binding energy *BE* as an input parameter.

Results and discussion

VMI of the CEP-controlled electron emission

Figure 2(a) and (b) shows typical single-shot momentum images measured with a sample containing 136 nm diameter ZnS nanoparticles. The laser propagation direction is along the *x*-axis and the laser is polarized along the *y*-axis. The images represent projections of the electron momentum distribution along the *z*-axis. It should be noted that we did not invert the images for our further analysis since this was not required for the comparison to the simulations and determination of the cut-off energies. The frames with nanoparticle signal are identified by a higher number of electron hits (see Figure 2(a)) compared to frames with signal from the background gas only (Figure 2(b)). Figure 2(c) and (d) shows the CEP-averaged images acquired over more than 1 million laser shots for nanoparticles and background gas, respectively. Note that the images have been corrected for a nonhomogeneous Microchannel Plate (MCP)-sensitivity and are left-right symmetrized for a better signal-to-noise ratio. We focus on the high-energy region and in particular the cut-off in the momentum spectra. The momentum distribution at high momenta in Figure 2(c) exhibits a dipolar character and is aligned along the laser polarization direction, in agreement with the previous work on SiO_2 nanoparticles (*14*). Inspection of Figure 2(c) and (d) already indicates a much higher cut-off for the nanoparticle signal when compared to the residual gas for otherwise identical laser parameters.

The CEP-dependence of the electron emission is analysed as outlined in earlier work on SiO_2 (*15*). For each (p_x,p_y)-momentum, the CEP-dependent electron signal

S was fitted with a sine-function with an amplitude A, a phase offset φ_0 (which is sometimes referred to as the 'phase of the phase' (*45*)), and a constant C_0 which accounts for any CEP-independent contributions:

$$S\left(p_x, p_y, \phi\right) = A\left(p_x, p_y\right) \sin\left(\phi + \varphi_0\left(p_x, p_y\right)\right) + C_0\left(p_y, p_y\right) \quad (1)$$

The resulting parameter A as a function of projected momenta p_x and p_y is shown in Figure 3(a). It is compared to the results from M³C simulations in Figure 3(b). We used the CEP-dependent electron emission to determine the cut-off of rescattered electrons in the experiment. The momentum where the amplitude A vanishes, and the phase offset φ_0 loses its well-defined oscillatory behaviour with CEP, is defined as the cut-off $p_c = \sqrt{2m_e E_c}$. A figure eight shape of the amplitude A is clearly visible in Figure 3(a) and (b), indicating that (i) the electron emission is dominated by rescattered electrons (*16*) and (ii) the highest energy electrons directly follow the direction of the strongest near-field components. In our earlier work on SiO_2, we found that the loss of direct electrons and dominance of rescattered electrons is a result of charge-interaction and the build-up of a trapping potential near the nanoparticle surface that traps all lower energy electrons (*14–16, 26, 46*). The rings in the simulations indicate the contributions from different sub-cycles of the laser pulse.

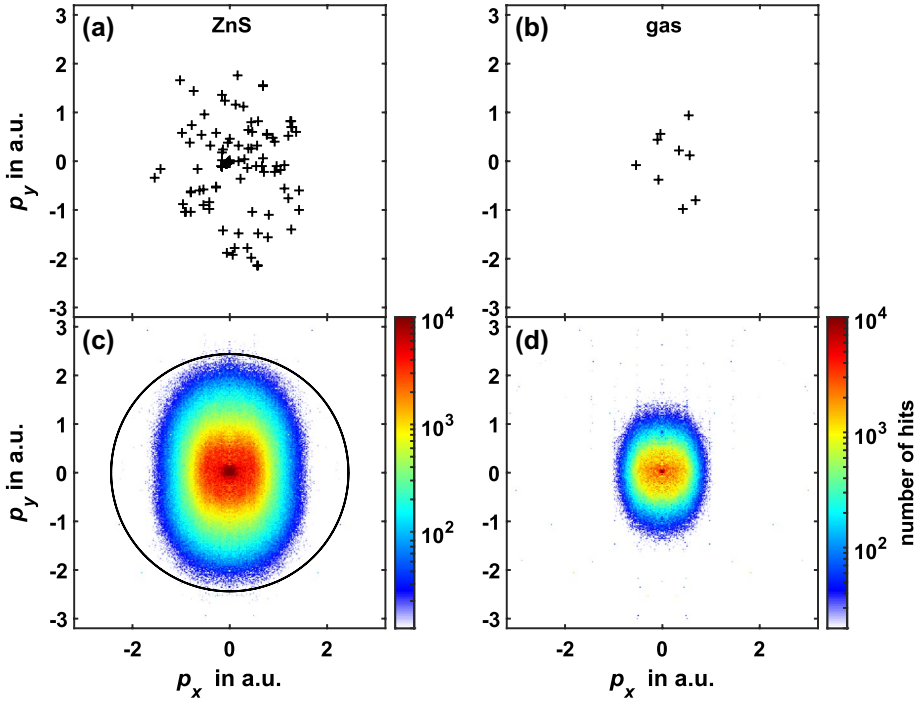

Figure 2. (a) and (b) Single shot images of a frame with (a) a ZnS nanoparticle and (b) residual gas obtained from measurements at a laser intensity of 1.5×10^{13} W/cm². (c) and (d) Projected photoelectron momentum distributions obtained by averaging over >1 million shots and all CEPs under the same conditions for (c) ZnS nanoparticles and (d) residual gas. The black circle indicates the cut-off momentum p_c retrieved from an analysis of the C.

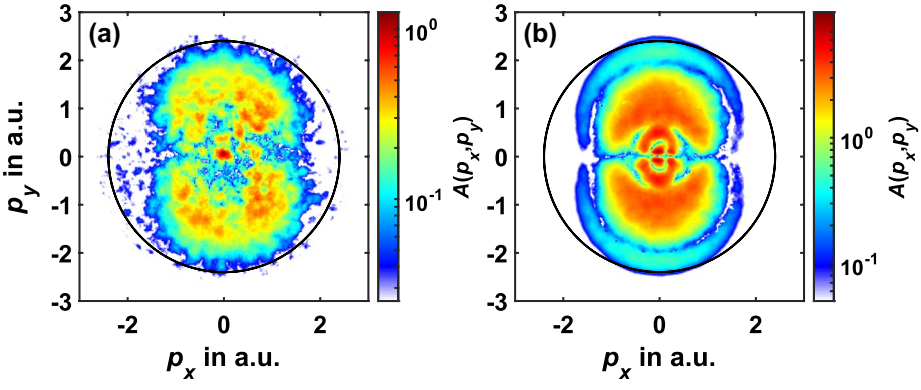

Figure 3. Momentum map of the amplitude A of the CEP-dependent part of the electron emission from ZnS nanoparticles obtained from (a) measurement at a laser intensity of 1.5×10^{13} W/cm² and (b) M³C simulations for the experimental parameters (including volume averaging). Black circles indicate the respective cut-off momenta.

Since the experimental low energy region is also affected by residual gas signal, we here concentrate on just the high-energy signal and the cut-off.

Intensity dependence of the electron emission from different materials

The intensity-dependent cut-off energy for electrons from nanoparticles of different materials is compared in Figure 4. The measurements with SiO_2 samples show a cut-off energy E_c around 50 U_p, in agreement with previous studies (*14*). Electrons from those nanoparticles with the largest permittivity and field enhancement (ZnS, Fe_3O_4) exhibit much higher cut-off energies of about 140 U_p. While the permittivity of polystyrene is similar to that of SiO_2, the cut-off energies measured for PS particles are significantly larger, especially at low intensities, suggesting that both the dielectric polarizability of the particle and the binding energy affect the electron acceleration process. In the experiment, the highest laser intensity was limited by the maximum electron kinetic energy detectable with the VMI spectrometer (~120 eV). The lowest intensity measurements were limited by the number of electrons emitted from the nanoparticles and the signal-to-noise ratio: with the 1-kHz laser source the lowest intensity measurements took 8 h, which is close to the limit of what can realistically be implemented while keeping the laser parameters constant.

The model simulations show overall good agreement with the experimental data, in particular for SiO_2 and PS nanoparticles, especially at higher intensities. Deviations for these nanoparticles at the lower intensity end might be caused by both limitations in the experiments and in the simulations. Experimentally, low electron emission numbers might favour particles with nano-protrusions, exhibiting higher field enhancement and thus higher photoemission probability. Without intrinsic diagnostics of the nanoparticles that contributed to the ionization signals, such a scenario cannot be excluded. We believe that this will be negligible at higher intensities. Theoretically, the description of the ionization step in the model becomes more challenging for lower intensities, where a transition to multi-photon ionization is expected and thus deviations from using a tunnelling ionization model could be expected.

Larger discrepancies in the cut-off energies for the ZnS and Fe_3O_4 can possibly be ascribed to significant deviation of the nanoparticle shape from a sphere for these samples. The M^3C simulations are expected to give quantitative results for spherical particles (see e.g. Refs. (*16, 26*)). Using the bulk binding energies for the different materials all major effects can be described, but we found the cut-off energies to be slightly too low at low intensities. The binding energies for nanoparticles can deviate from their bulk values due to the inclusion of impurities, which is known for SiO_2 to lower the binding energy (see Table 1). In cases where the binding energies for nanoparticles were unknown, we adapted their values from the reported bulk values within the same range found for silica (about 20%) for optimal agreement with the experimental data. The curves shown in Figure 4 were obtained assuming the binding energies for nanoparticles as given in Table 1.

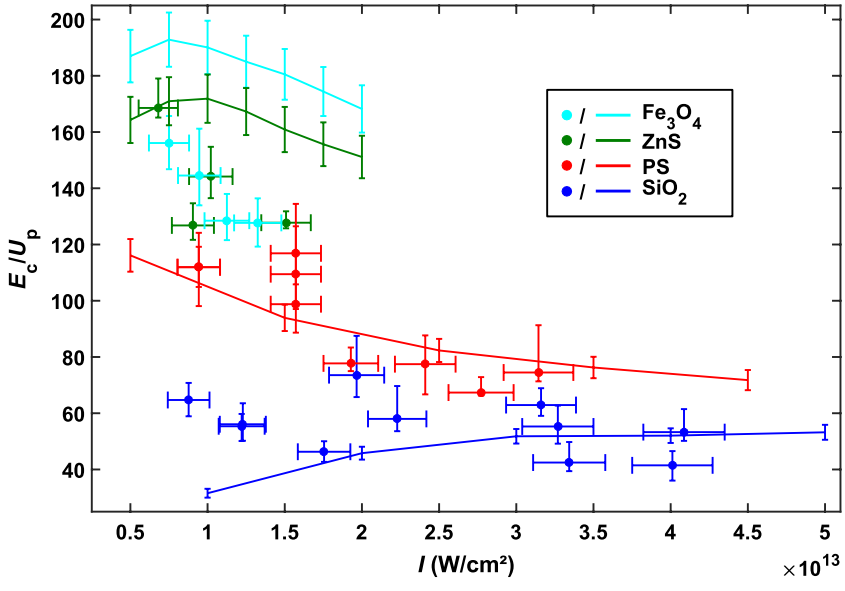

Figure 4. Laser intensity dependence of the cut-off energy E_c/U_p measured in SiO_2 (blue dots), polystyrene (PS) (red dots), ZnS (green dots) and Fe_3O_4 (cyan dots) nanoparticles. The results of M^3C model simulations for spherical particles are shown as solid lines. Error bars correspond to uncertainties in determining the cut-off values and laser intensities.

An increase in the cut-off energy with increasing ε_r can be intuitively explained by the dependence of the near-field enhancement on the permittivity. For a neutral dielectric sphere in vacuum, Mie theory predicts a monotonous increase in the field enhancement factor with permittivity as illustrated for the four studied materials in Table 1.

The dependence of the electron cut-off energy on the binding energy is more complex and can be related to the influence of the binding energy on the electron tunnelling process. On the one hand, the binding energy determines the position of the electron tunnelling exit. As the electron dynamics is very sensitive to the initial displacement of the tunnelled electron with respect to the parent ion, this change can affect the electron cut-off energies. On the other hand, the binding energy has a direct effect on the ionization rate and thus on the number of the released electrons and residual ions. With increasing binding energy, the density of free charges decreases resulting in reduction of the many-particle field and correspondingly in a lower contribution to the acceleration of electrons.

To explore the general dependence of the photoemission process on the electron binding energy *BE* of the material, we performed M^{3}C simulations for a set of values within the range 4.0eV < BE < 10.0eV covering the spectrum of most dielectrics and semiconductors. The colour map in Figure 5 shows the cut-off energies, scaled to the ponderomotive potential of the enhanced surface field, $E_c/(\alpha^2 U_p)$, as a function of the binding energy *BE* and the dielectrically enhanced intensity at the surface of the particle $\alpha^2 I$. It should be emphasized that the normalization to the linear field enhancement in this analysis would lead to a constant cut-off energy in terms of U_p if the effects of the tunnel exit and charge interaction would be negligible. The results of the simulations, however, reveal a quite complex behaviour. For the lowest dielectrically enhanced surface intensities ($\alpha^2 I \lesssim 4 \times 10^{13}$ W/cm^2), the scaled cut-off energy shows a significant dependence on binding energy, where the values decrease with increasing binding energy. This can be explained by a higher ionization rate and correspondingly stronger many-particle Coulomb field for lower binding energies at these intensities. In addition, a closer tunnelling exit in case of lower binding energies can contribute to the observed dependence. As intensity increases, the density of the ionized electrons in the vicinity of the particle reaches a critical value and the mean-field starts screening the driving field. This diminishes the dependence on binding energy because the mean-field limits the total number of created charges and compensates for differences during the ionization process. In this regime, the scaled cut-off energy shows very small intensity dependence with values in the range of 20–25 and the material dependence is effectively quenched.

Having identified the dependence of the scaled cut-off energy on the material parameters, we now examine the relative contributions of the linear field enhancement and the mean-field to the electron acceleration process

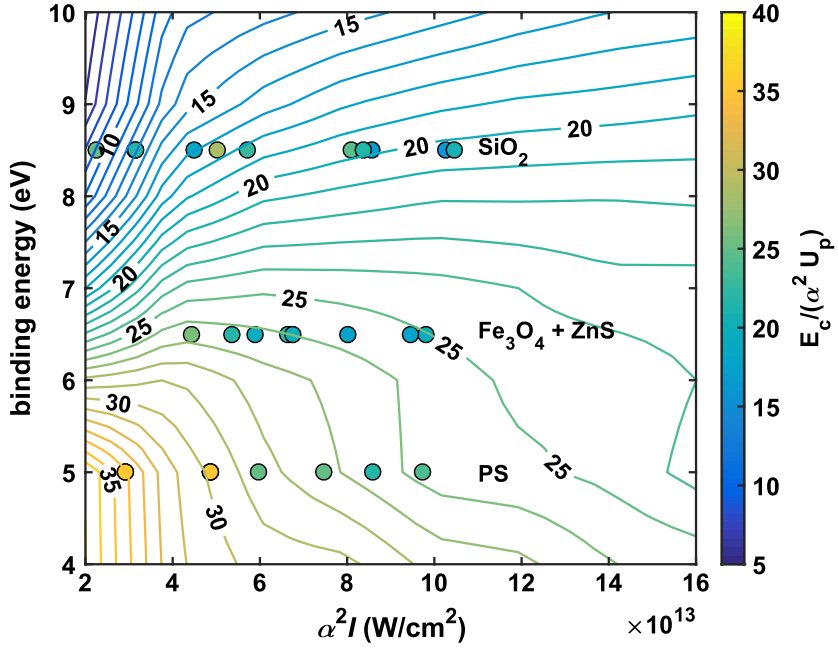

Figure 5. Dependence of the scaled electron cut-off energies, $E_c/(\alpha^2 U_p)$, on the binding energy *BE* and dielectrically enhanced surface intensity, $\alpha^2 I$, obtained from M^{3}C simulations. In the simulations 100 nm SiO_2 nanoparticle parameters were assumed and the laser intensity was varied in the range of 0.8–6.25 × 10^{13} W/cm^2. The circles represent experimental results from the four investigated materials and are coloured according to the measured scaled cut-off values.

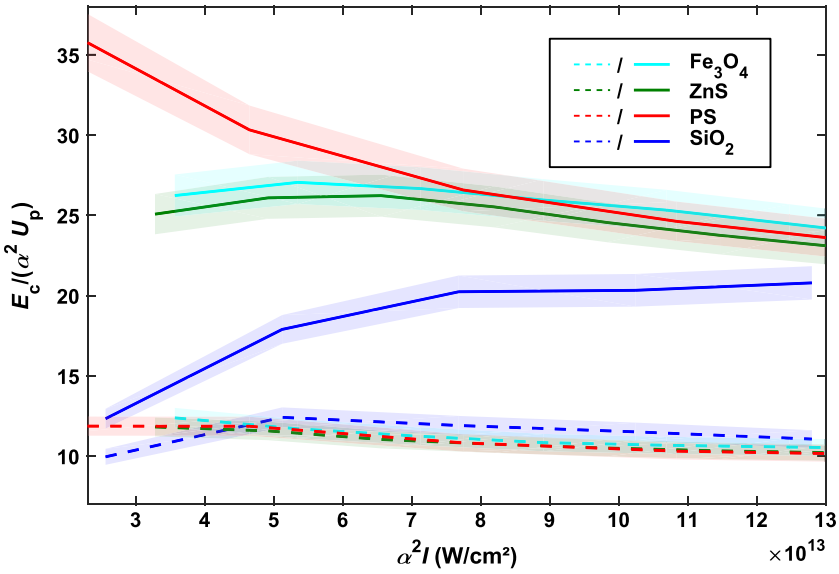

Figure 6. Scaled cut-off energies obtained from M³C simulations for SiO_2, PS, ZnS and Fe_3O_4 nanoparticles with the mean-field turned off (dashed lines) and on (solid lines). Shaded areas visualize the error bars resulting from the determination of the cut-offs.

in different materials. For each material, we performed (1) full M³C simulations and (2) simulations with the mean-field switched off. To account for the difference in the field enhancement factors of the materials, the scaled cut-off energy was plotted as a function of the dielectrically enhanced surface intensity $\alpha^2 I$. When neglecting the charge interaction all the materials show quite similar intensity scaling close to the semi-classical atomic cut-off law (cf. Figure 6, dashed lines: $E_{c,no\_mf} \approx 10\ \alpha^2 U_p$). Including charge interaction results in a significant increase in the scaled cut-off energies (solid lines). Though different materials show significant deviation at low intensities they converge as the intensity increases. While the values for PS, ZnS and Fe_3O_4 already converge at around 8×10^{13} W/cm², SiO_2 with the highest binding energy lies at this intensity within a 20% range and gets closer with increasing intensity.

The weak intensity and material dependence above an enhanced surface intensity of 8×10^{13} W/cm² can be explained by the build-up of the mean-field from charge interaction and subsequent screening of the driving laser field leading to quenching of additional ionization. In agreement with this explanation, the number of emitted electrons is only linearly increasing with intensity, whereas an exponential increase would be expected without charge interaction.

Conclusions

We have studied electron emission in nanolocalized fields of isolated nanoparticles of different materials. Comparison with trajectory-based M³C simulations shows that the permittivity and binding energy of the material are the main parameters that determine the material-dependent contribution to the electron acceleration process. Similar to the previous studies, both dielectrically enhanced near field and the fields resulting from the interaction with released electrons and residual ions contribute to the acceleration dynamics. Our results for particles in the size range of 100 nm clearly show the quenching effect that marks the transition from the tunnel-rate driven to purely Coulomb-limited behaviour in the acceleration dynamics. We expect that this conclusion also holds for other materials, providing predictive capability for the cut-off energies that can be obtained in electron acceleration in strong near-fields of nanoscale materials under charge interaction. Our results may also be of relevance in applications of nanosystems for the generation of ultrashort electron bunches.

Disclosure statement

No potential conflict of interest was reported by the authors.

Funding

We are grateful for support by the Max Planck Society and the DFG through SPP1840 (QUTIF), SPP1391 and the Cluster of Excellence: Munich-Centre for Advanced Photonics (MAP). We also acknowledge support from the EU via the ERC grant ATTOCO (grant number 307203). This research has been supported in part by Global Research Laboratory Program [grant no 2009-00439] and by Max Planck POSTECH/KOREA Research Initiative Program [grant no 2016K1A4A4A01922028] through the National Research Foundation of Korea (NRF) funded by Ministry of Science, ICT & Future Planning. The

Berlin group of this research has been supported by the BMBF (05K13KE2).

References

(1) Schiffrin, A.; Paasch-Colberg, T.; Karpowicz, N.; Apalkov, V.; Gerster, D.; Muhlbrandt, S.; Korbman, M.; Reichert, J.; Schultze, M.; Holzner, S.; Barth, J.V.; Kienberger, R.; Ernstorfer, R.; Yakovlev, V.S.; Stockman, M.I.; Krausz, F. Optical-field-induced Current in Dielectrics. *Nature* **2013**, *493,* 70–74.

(2) Schultze, M.; Bothschafter, E.M.; Sommer, A.; Holzner, S.; Schweinberger, W.; Fiess, M.; Hofstetter, M.; Kienberger, R.; Apalkov, V.; Yakovlev, V.S.; Stockman, M.I.; Krausz, F. Controlling Dielectrics with the Electric Field of Light. *Nature* **2013**, *493,* 75–78.

(3) Schultze, M.; Ramasesha, K.; Pemmaraju, C.D.; Sato, S.A.; Whitmore, D.; Gandman, A.; Prell, J.S.; Borja, L.J.; Prendergast, D.; Yabana, K.; Neumark, D.M.; Leone, S.R. Attosecond Band-gap Dynamics in Silicon. *Science* **2014**, *346,* 1348–1352.

(4) Durach, M.; Rusina, A.; Kling, M.F.; Stockman, M.I. Predicted Ultrafast Dynamic Metallization of Dielectric Nanofilms by Strong Single-cycle Optical Fields. *Phys. Rev. Lett.* **2011**, *107,* 086602.

(5) Krausz, F.; Stockman, M.I. Attosecond Metrology: From Electron Capture to Future Signal Processing. *Nat. Photonics* **2014**, *8,* 205–213.

(6) Locher, R.; Castiglioni, L.; Lucchini, M.; Greif, M.; Gallmann, L.; Osterwalder, J.; Hengsberger, M.; Keller, U. Energy-dependent Photoemission Delays from Noble Metal Surfaces by Attosecond Interferometry. *Optica* **2015**, *2,* 405–410.

(7) Neppl, S.; Ernstorfer, R.; Cavalieri, A.L.; Lemell, C.; Wachter, G.; Magerl, E.; Bothschafter, E.M.; Jobst, M.; Hofstetter, M.; Kleineberg, U.; Barth, J.V.; Menzel, D.; Burgdorfer, J.; Feulner, P.; Krausz, F.; Kienberger, R. Direct Observation of Electron Propagation and Dielectric Screening on the Atomic Length Scale. *Nature* **2015**, *517,* 342–346.

(8) Förg, B.; Schötz, J.; Süßmann, F.; Förster, M.; Krüger, M.; Ahn, B.; Okell, W.A.; Wintersperger, K.; Zherebtsov, S.; Guggenmos, A.; Pervak, V.; Kessel, A.; Trushin, S.A.; Azzeer, A.M.; Stockman, M.I.; Kim, D.; Krausz, F.; Hommelhoff, P.; Kling, M.F. Attosecond Nanoscale Near-field Sampling. *Nat. Commun.* **2016**, *7,* 11717.

(9) Skopalova, E.; Lei, D.Y.; Witting, T.; Arrell, C.; Frank, F.; Sonnefraud, Y.; Maier, S.A.; Tisch, J.W.G.; Marangos, J.P. Numerical Simulation of Attosecond Nanoplasmonic Streaking. *New J. Phys.* **2011**, *13,* 083003.

(10) Stockman, M.I.; Kling, M.F.; Kleineberg, U.; Krausz, F. Attosecond Nanoplasmonic-field Microscope. *Nat. Photonics* **2007**, *1,* 539–544.

(11) Süßmann, F.; Kling, M.F. Attosecond Nanoplasmonic Streaking of Localized Fields near Metal Nanospheres. *Phys. Rev. B* **2011**, *84,* 121406(R).

(12) Krüger, M.; Schenk, M.; Hommelhoff, P. Attosecond Control of Electrons Emitted from a Nanoscale Metal Tip. *Nature* **2011**, *475,* 78–81.

(13) Wachter, G.; Lemell, C.; Burgdörfer, J.; Schenk, M.; Krüger, M.; Hommelhoff, P. Electron Rescattering at Metal Nanotips Induced by Ultrashort Laser Pulses. *Phys. Rev. B* **2012**, *86,* 035402.

(14) Zherebtsov, S.; Fennel, T.; Plenge, J.; Antonsson, E.; Znakovskaya, I.; Wirth, A.; Herrwerth, O.; Süßmann, F.; Peltz, C.; Ahmad, I.; Trushin, S.; Pervak, V.; Karsch, S.; Vrakking, M.J.J.; Langer, B.; Graf, C.; Stockman, M.I.; Krausz, F.; Rühl, E.; Kling, M.F. Controlled Near-field Enhanced Electron Acceleration from Dielectric Nanospheres with Intense Few-cycle Laser Fields. *Nat. Phys.* **2011**, *7,* 656–662.

(15) Zherebtsov, S.; Süßmann, F.; Peltz, C.; Plenge, J.; Betsch, K.J.; Znakovskaya, I.; Alnaser, A.S.; Johnson, N.G.; Kübel, M.; Horn, A.; Mondes, V.; Graf, C.; Trushin, S.; Azzeer, A.; Vrakking, M.J.J.; Paulus, G.G.; Krausz, F.; Rühl, E.; Fennel, T.; Kling, M.F. Carrier-Envelope Phase-tagged Imaging of the Controlled Electron Acceleration from SiO_2 Nanospheres in Intense Few-cycle Laser Fields. *New J. Phys.* **2012**, *14,* 075010.

(16) Süßmann, F.; Seiffert, L.; Zherebtsov, S.; Mondes, V.; Stierle, J.; Arbeiter, M.; Plenge, J.; Rupp, P.; Peltz, C.; Kessel, A.; Trushin, S.A.; Ahn, B.; Kim, D.; Graf, C.; Rühl, E.; Kling, M.F.; Fennel, T. Field Propagation-induced Directionality of Carrier-envelope Phase-controlled Photoemission from Nanospheres. *Nat. Commun.* **2015**, *6,* 8944.

(17) Herink, G.; Solli, D.R.; Gulde, M.; Ropers, C. Field-driven Photoemission from Nanostructures Quenches the Quiver Motion. *Nature* **2012**, *483,* 190–193.

(18) Piglosiewicz, B.; Schmidt, S.; Park, D.J.; Vogelsang, J.; Grosz, P.; Manzoni, C.; Farinello, P.; Cerullo, G.; Lienau, C. Carrier-envelope Phase Effects on the Strong-field Photoemission of Electrons from Metallic Nanostructures. *Nat. Photonics* **2014**, *8,* 37–42.

(19) Yanagisawa, H.; Schnepp, S.; Hafner, C.; Hengsberger, M.; Kim, D.E.; Kling, M.F.; Landsman, A.; Gallmann, L.; Osterwalder, J. Delayed Electron Emission in Strong-field Driven Tunnelling from a Metallic Nanotip in the Multi-electron Regime. *Sci. Rep.* 2016, *6*, 35877.

(20) Vogelsang, J.; Robin, J.; Nagy, B.J.; Dombi, P.; Rosenkranz, D.; Schiek, M.; Groß, P.; Lienau, C. Ultrafast Electron Emission from a Sharp Metal Nanotaper Driven by Adiabatic Nanofocusing of Surface Plasmons. *Nano Lett.* **2015**, *15,* 4685–4691.

(21) Dombi, P.; Hörl, A.; Rácz, P.; Márton, I.; Trügler, A.; Krenn, J.R.; Hohenester, U. Ultrafast Strong-field Photoemission from Plasmonic Nanoparticles. *Nano Lett.* **2013**, *13,* 674–678.

(22) Rácz, P.; Irvine, S.E.; Lenner, M.; Mitrofanov, A.; Baltuška, A.; Elezzabi, A.Y.; Dombi, P. Strong-Field Plasmonic Electron Acceleration with Few-cycle, Phase-stabilized Laser Pulses. *Appl. Phys. Lett.* **2011**, *98,* 111116.

(23) Paulus, G.G.; Nicklich, W.; Xu, H.; Lambropoulos, P.; Walther, H. Plateau in Above Threshold Ionization Spectra. *Phys. Rev. Lett.* **1994**, *72,* 2851–2854.

(24) Corkum, P.B. Plasma Perspective on Strong Field Multiphoton Ionization. *Phys. Rev. Lett.* **1993**, *71,* 1994–1997.

(25) Summers, A.M.; Ramm, A.S.; Paneru, G.; Kling, M.F.; Flanders, B.N.; Trallero-Herrero, C.A. Optical Damage Threshold of Au Nanowires in Strong Femtosecond Laser Fields. *Opt. Express* **2014**, *22,* 4235–4246.

(26) Seiffert, L.; Süßmann, F.; Zherebtsov, S.; Rupp, P.; Peltz, C.; Rühl, E.; Kling, M.F.; Fennel, T. Competition of Single and Double Rescattering in the Strong-field Photoemission from Dielectric Nanospheres. *Appl. Phys. B* **2016**, *122,* 1–9.

(27) Wilson, K.R.; Zou, S.; Shu, J.; Ruhl, E.; Leone, S.R.; Schatz, G.C.; Ahmed, M. Size-dependent Angular Distributions of Low-energy Photoelectrons Emitted from NaCl Nanoparticles. *Nano Lett.* **2007**, *7,* 2014–2019.
(28) Wittmann, T.; Horvath, B.; Helml, W.; Schätzel, M.G.; Gu, X.; Cavalieri, A.L.; Paulus, G.G.; Kienberger, R. Single-shot Carrier–Envelope Phase Measurement of Few-cycle Laser Pulses. *Nat. Phys.* **2009**, *5,* 357–362.
(29) Rathje, T.; Johnson, N.G.; Möller, M.; Süßmann, F.; Adolph, D.; Kübel, M.; Kienberger, R.; Kling, M.F.; Paulus, G.; Sayler, A. Review of Attosecond Resolved Measurement and Control via Carrier–Envelope Phase Tagging with Above-threshold Ionization. *J. Phys. B: At. Mol. Opt. Phys.* **2012**, *45,* 074003.
(30) Süßmann, F.; Zherebtsov, S.; Plenge, J.; Johnson, N.G.; Kübel, M.; Sayler, A.M.; Mondes, V.; Graf, C.; Rühl, E.; Paulus, G.G.; Schmischke, D.; Swrschek, P.; Kling, M.F. Single-shot Velocity-map Imaging of Attosecond Light-field Control at Kilohertz Rate. *Rev. Sci. Instrum.* **2011**, *82,* 093109.
(31) Busuladžić, M.; Gazibegović-Busuladžić, A.; Milošević, D.B. High-Order above-Threshold Ionization in a Laser Field: Influence of the Ionization Potential on the High-Energy Cutoff. *Laser Physics* **2006**, *16,* 289–293.
(32) Stöber, W.; Fink, A.; Bohn, E. Controlled Growth of Monodisperse Silica Spheres in the Micron Size Range. *J. Colloid Interface Sci.* **1968**, *26,* 62–69.
(33) Schäfer, C.G.; Gallei, M.; Zahn, J.T.; Engelhardt, J.; Hellmann, G.t.P.; Rehahn, M. Reversible Light-, Thermo-, and Mechano-Responsive Elastomeric Polymer Opal Films. *Chem. Mater.* **2013**, *25,* 2309–2318.
(34) Han, M.G.; Shin, C.G.; Jeon, S.J.; Shim, H.; Heo, C.J.; Jin, H.; Kim, J.W.; Lee, S. Full Color Tunable Photonic Crystal from Crystalline Colloidal Arrays with an Engineered Photonic Stop-Band. *Adv. Mater.* **2012**, *24,* 6438–6444.
(35) Cheng, C.; Wen, Y.; Xu, X.; Gu, H. Tunable Synthesis of Carboxyl-Functionalized Magnetite Nanocrystal Clusters with Uniform Size. *J. Mater. Chem.* **2009**, *19,* 8782–8788.
(36) Antonsson, E. Photoexcitation, Photoionization, and X-Ray Scattering of Free Nanoparticles Prepared in a Beam. Ph.D. Dissertation, Freie Universität Berlin, 2011.
(37) DiStefano, T.H.; Eastman, D.E. The Band Edge of Amorphous SiO_2 by Photoinjection and Photoconductivity Measurements. *Solid State Commun.* **1971**, *9,* 2259–2261.
(38) Duke, C.B.; Salaneck, W.R.; Fabish, T.J.; Ritsko, J.J.; Thomas, H.R.; Paton, A. Electronic Structure of Pendant-group Polymers: Molecular-ion States and Dielectric Properties of Poly(2-Vinyl Pyridine). *Phys. Rev. B* **1978**, *18,* 5717–5739.
(39) Fujihira, M.; Hirooka, T.; Inokuchi, H. Photoemission from Compounds Containing Benzene, Naphtalene and Anthracene Ring Systems. *Chem. Phys. Lett.* **1973**, *19* (4), 584–587.
(40) Swank, R.K. Surface Properties of II–VI Compounds. *Phys. Rev.* **1967**, *153,* 844–849.
(41) Fonin, M.; Pentcheva, R.; Dedkov, Y.S.; Sperlich, M.; Vyalikh, D.V.; Scheffler, M.; Rüdiger, U.; Güntherodt, G. Surface Electronic Structure of the Fe_3O_4(100): Evidence of a Half-metal to Metal Transition. *Phys. Rev. B* **2005**, *72,* 104436.
(42) Ammosov, M.; Delone, N.; Krainov, V. Tunnelling Ionization of Complex Atoms and of Atomic Ions in an Alternating Electromagnetic Field. *Sov. Phys. JETP* **1986**, *64,* 1191–1194.
(43) Assimos, J.A.; Trivich, D. The Photoelectric Threshold, Work Function, and Surface Barrier Potential of Single-crystal Cuprous Oxide. *Phys. Status Solidi A* **1974**, *26,* 477–488.
(44) Lotz, W. An Empirical Formula for the Electron-impact Ionization Cross-Section. *Z. Phys.* **1967**, *206,* 205–211.
(45) Skruszewicz, S.; Tiggesbäumker, J.; Meiwes-Broer, K.-H.; Arbeiter, M.; Fennel, T.; Bauer, D. Two-color Strong-field Photoelectron Spectroscopy and the Phase of the Phase. *Phys. Rev. Lett.* **2015**, *115,* 043001.
(46) Seiffert, L.; Henning, P.; Rupp, P.; Zherebtsov, S.; Hommelhoff, P.; Kling, M.F.; Fennel, T. Trapping Field Assisted Backscattering in the Strong-field Photoemission from Dielectric Nanospheres. *J. Mod. Opt.*, submitted.